Pergamon

Int. J. Heat Mass Transfer. Vol. 40, No. 2, pp. 223–235, 1997

0017–9310/97 $15.00+0.00

PII: S0017–9310(96)00127–5

Buoyancy-force-driven transitions in flow structures and their effects on heat transfer in a rotating curved channel

LIQIU WANG†

School of Mechanical and Production Engineering, Nanyang Technological University, Singapore 639798

(*Received* 22 *December* 1995 *and in final form* 9 *April* 1996)

Abstract—Buoyancy-force-driven transitions in flow structures are examined numerically by a finite volume method. The specific problem considered is a steady, hydrodynamically and thermally fully developed flow in a square channel with streamwise curvature, spanwise rotation and wall heating or cooling. The buoyancy force is found to significantly affect the flow structures and heat transfer. Several previously unknown phenomena are revealed. Results include both transitions in flow structures and effects of the flow transitions on flow resistance and heat transfer. Copyright © 1996 Elsevier Science Ltd.

1. INTRODUCTION

Buoyancy forces arise as a result of variations of density in a fluid subject to a force field, and produce a wide range of phenomena of importance in various practical problems. In this work, the phenomena encountered are examined for steady, hydrodynamically and thermally fully developed flow in a rotating curved channel with a square cross section. Flow geometry is shown in Fig. 1 with (R, Z, ϕ) as normal (radial), spanwise and streamwise directions, respectively. A viscous fluid is driven by a streamwise pressure gradient to flow through a square channel with a streamwise curvature, spanwise rotation, and streamwisely and peripherally uniform wall heating or cooling. Such a geometry appears in cooling systems for conductors of electric generators. It is also employed in applications such as separation processes and rotating heat exchangers. Studying a rotating curved channel flow may thus lead to a better understanding of flow and heat transfer in these devices.

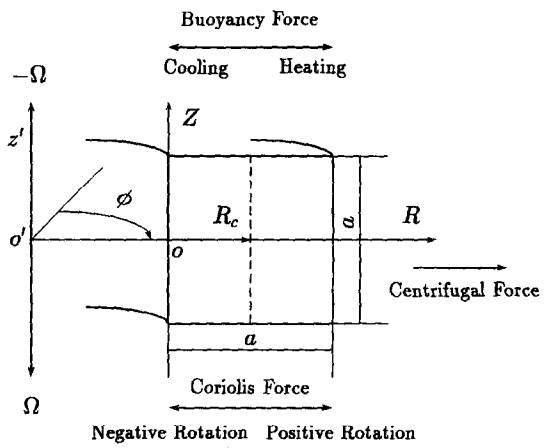

Fig. 1. Pressure-driven flow in a square channel with curvature, rotation and heating/cooling.

Rotation and heating/cooling of a channel generates a centrifugal force field and a density variation of the fluid. This results in a buoyancy force on a plane perpendicular to the axis of the channel (cross plane, RZ-plane). Depending on whether fluid is heated or cooled, this buoyancy force can be either positive or negative R-directed, and thus enhances or counteracts centrifugal and Coriolis forces due to the curvature and rotation. Nonlinear interaction of the buoyancy force with the other forces results in a complicated flow structure. We examine this structure in the present study using a finite volume scheme.

Because of complexities of the problem, early works on rotating curved channel flows have been constrained to some simplified limiting cases in which either centrifugal force or Coriolis force dominates. Ludwieg (1951) [1] and Hocking (1967) [2] developed a solution based on a momentum integral method for the fully developed flow in a square and rectangular channel with a strong spanwise rotation. Miyazaki [3, 4] examined the fully developed laminar flow and heat transfer in a curved circular/rectangular channel with spanwise rotation and heating effect by a finite difference method. Because of convergence difficulties with the iterative method used, Miyazaki's work was constrained to the case of weak curvature, rotation and heating rates. Since the solution is only for the asymptotic cases, the secondary flow revealed by these early works consists of one-pair of counter-rotating vortices in the cross plane. The interaction of secondary flow with pressure-driven main flow shifts location of the

† Present address: Department of Mechanical Engineering, University of Hong Kong, Hong Kong.

NOMENCLATURE

a width and height of the square channel
c_1 streamwise pressure gradient, $-\partial P'/R_c\partial\phi$
c_2 streamwise temperature gradient, $\partial T/R_c\partial\phi$
De Dean number, $Re\sqrt{\sigma}$
Dk pseudo Dean number, $\sigma a W_1/4\nu$
fRe, Nu friction factor × Reynolds number, Nusselt number
$(fRe)_0$ friction factor × Reynolds number for a stationary straight square channel, 14.23
L_1, L_2 dimensionless parameters, $L_1 = 3Re_\Omega/2Dk$, $L_2 = Ra_\Omega/16Dk$
Nu_0 Nusselt number for a stationary straight square channel, 3.608
Pr Prandtl number, ν/α
r, z dimensionless coordinates, $r = R/a$, $z = Z/a$
Ra_Ω rotational Rayleigh number, $\beta R_c\Omega^2 a^3\Delta T/\nu^2$
R_c curvature radius
Re Reynolds number, $W_m a/\nu$
Re_Ω rotational Reynolds number, $a^2\Omega/\nu$
Ro rotation number, $\Omega a/W_m$
p' fluid pressure
P pseudo pressure, $p' - \rho[R-a/2+(R-a)^2/(2R_c)]R_c\Omega^2$
T, T_w temperature of fluid and wall
U, V, W velocity components in the directions of R, Z and ϕ
u, v, w, p, t dimensionless variables, $u = aU/\nu$, $v = aV/\nu$, $w = W/W_1$, $p = P/\rho(\nu/a)^2$, $t = (T_w - T)/\Delta T$
W_m, T_b mean streamwise velocity and bulk mean temperature
w_m, t_b dimensionless mean streamwise velocity and bulk mean temperature
w_{max}, t_{max} maximum values of w and t
W_1 representative streamwise velocity, $a^2 c_1/\mu$
R, Z, ϕ coordinates.

Greek symbols

α thermal diffusivity
β coefficient of thermal expansion
μ viscosity of fluid
ν kinematic viscosity of fluid
Ω angular velocity
ψ non-dimensional stream function
$|\psi|_{max}$ maximum value of $|\psi|$
ρ density of fluid based on wall temperature
σ curvature ratio, a/R_c
ΔT representative temperature difference, $Prac_2$

maximum streamwise velocity away from the center of channel and in the direction of secondary velocities in the middle of channel.

More comprehensive studies have been made in Refs. [5–7]. Selmi *et al.* [5] numerically examined the combined effects of spanwise rotation (Coriolis force) and curvature (centrifugal force) on the bifurcation structure of fully developed flows in a rectangular channel. Matsson and Alredsson [6] visualized and measured the flow in a curved air channel with a high aspect ratio and a spanwise rotation using smoke visualization and hotwire measurements, with emphasis on the effect of spanwise rotation on primary and secondary instabilities in curved channel flow. The stability analysis in Ref. [7] revealed that there are two potentially unstable regions alternating with two stable layers in the cross plane for the flows in a curved channel with a low negative spanwise rotation. The flow visualization in Ref. [7] showed that competition of two destabilizing mechanisms due to the curvature and rotation, respectively, causes appearance of multiple pairs of vortices. Note that all these works have imposed an isothermal condition. Thus questions concerning effect of the buoyancy force have been left unanswered.

In this work, buoyancy-force-driven transitions in flow structures are examined for the rotating curved channel flow by a finite volume method. Also investigated is the effect of flow transitions on distributions of temperature, friction factor and Nusselt number. The work is thus of fundamental interest regarding both effects of heat transfer on flow structure and effects of flow structure transition on heat transfer in addition to its practical interest. The specific problem considered here is the fully developed laminar flow in a square channel (Fig. 1) with a uniform wall heat flux and peripherally uniform wall temperature. The solution covers both heating and cooling cases.

2. GOVERNING EQUATIONS AND NUMERICAL METHOD

Consider a steady, hydrodynamically and thermally fully developed flow in a square channel with streamwise curvature, spanwise rotation, and wall heating or cooling at a constant heat flux (Fig. 1). The geometry is toroidal and hence finite pitch effect is not considered. The rotation can be *positive* or *negative* at a constant angular velocity Ω. A positive rotation gives rise to a Coriolis force in the cross plane directed along positive R-direction and vice versa. The channel is streamwisely and peripherally uniformly heated or

cooled with a uniform peripheral temperature. The properties of fluid, with the exception of density, are taken to be constant. The gravitational force is negligible compared with the centrifugal and Coriolis forces.

Consider a non-inertial toroidal coordinate system (R, Z, ϕ) fixed to the curved channel rotating with a constant angular velocity Ω about the $o'z'$ axis, as shown in Fig. 1. Direction of the main flow is chosen in the direction of increasing ϕ, while the angular velocity of the channel is taken as $\Omega > 0$ for increasing ϕ (positive rotation) and $\Omega < 0$ for decreasing ϕ (negative rotation), respectively. Continuity, Navier–Stokes and energy equations governing the fully-developed laminar flow and heat transfer are given, in terms of the dimensionless variables, as [3, 4]:

continuity equation

$$\frac{\partial}{\partial r}\{[1+\sigma(r-0.5)]u\}+\frac{\partial}{\partial z}\{[1+\sigma(r-0.5)]v\}=0 \tag{1}$$

momentum equations

$$u\frac{\partial u}{\partial r}+v\frac{\partial u}{\partial z}-\frac{16Dk^2w^2}{\sigma[1+\sigma(r-0.5)]}-\frac{4L_1Dk^2w}{3\sigma}-16DkL_2[1+\sigma(r-0.5)]t=-\frac{\partial p}{\partial r}+\left\{\frac{\partial^2 u}{\partial r^2}+\frac{\partial^2 u}{\partial z^2}+\frac{\sigma}{1+\sigma(r-0.5)}\frac{\partial u}{\partial r}-\frac{\sigma^2 u}{[1+\sigma(r-0.5)]^2}\right\} \tag{2}$$

$$u\frac{\partial v}{\partial r}+v\frac{\partial v}{\partial z}=-\frac{\partial p}{\partial z}+\left[\frac{\partial^2 v}{\partial r^2}+\frac{\partial^2 v}{\partial z^2}+\frac{\sigma}{1+\sigma(r-0.5)}\frac{\partial v}{\partial r}\right] \tag{3}$$

$$u\frac{\partial w}{\partial r}+v\frac{\partial w}{\partial z}+\frac{\sigma uw}{1+\sigma(r-0.5)}+\frac{\sigma L_1 u}{12}=\frac{1}{1+\sigma(r-0.5)}+\left\{\frac{\partial^2 w}{\partial r^2}+\frac{\partial^2 w}{\partial z^2}+\frac{\sigma}{1+\sigma(r-0.5)}\frac{\partial w}{\partial r}-\frac{\sigma^2 w}{[1+\sigma(r-0.5)]^2}\right\} \tag{4}$$

energy equation

$$u\frac{\partial t}{\partial r}+v\frac{\partial t}{\partial z}-\frac{4Dkw}{\sigma Pr[1+\sigma(r-0.5)]}=\frac{1}{Pr}\left[\frac{\partial^2 t}{\partial r^2}+\frac{\partial^2 t}{\partial z^2}+\frac{\sigma}{1+\sigma(r-0.5)}\frac{\partial t}{\partial r}\right] \tag{5}$$

in which usual Boussinesq approximation is used to deal with the density variation. The dimensionless variables and parameters are defined in the nomenclature.

It is customary to use mean streamwise velocity W_m and difference between wall temperature and bulk mean temperature $(T_w - T_b)$ for the non-dimensionlization of streamwise velocity and temperature, respectively. However, employment of these quantities results unavoidably in appearance of two unknown dimensionless parameters which comprise the unknowns W_m and T_b, respectively. Consequently, an iterative procedure should be applied, assuming some initial estimated values to them. It requires an additional computation time. To avoid this additional increase in computation time, we follow Miyazaki [3, 4] in using W_1 and ΔT as the representative streamwise velocity and the representative temperature difference, respectively. They involve streamwise pressure gradient c_1 and streamwise temperature gradient c_2, which are usually given as design parameters so that it does not cause a problem in using computation results for design. The velocity W_1 is proportional to the pressure drop in the streamwise direction. For flows in a stationary straight circular tube, mean streamwise velocity W_m is related to W_1 as $W_m = W_1/8$ [3, 4]. The temperature difference ΔT is, on the other hand, proportional to the fluid temperature difference between channel inlet and outlet.

Dimensionless groups adopted here are those in refs. [3, 4, 8]. Curvature ratio σ is a geometry parameter, representing the degree of curvature. Prandtl number Pr, a thermophysical property parameter, represents the ratio of momentum diffusion rate to that of thermal diffusion. Dk is a pseudo Dean number with W_1 as the characteristic velocity [3, 4]. Rotational Reynolds number Re_Ω emerges from Coriolis term of momentum equations. It indicates ratio of Coriolis force to viscous force. A positive Re_Ω represents the case of positive rotation. A negative Re_Ω is for the negative rotation. It is noted that in the literature the rotational Reynolds number is also known as Taylor number or reciprocal of Ekman number. It is adopted here instead of the Ekman number because an increase in Re_Ω implies growth of the Coriolis force, and its effects are more readily conceivable (in particular for the limiting case as $\Omega \to 0$). Rotational Rayleigh number Ra_Ω has its origin in centrifugal buoyancy terms. It is similar to the Rayleigh number Ra encountered in the study of gravitational buoyancy force due to the earth's gravitational field, but with the gravitational acceleration replaced by the centrifugal acceleration measured at the centerline of the channel. It denotes ratio of centrifugal-type buoyancy force to viscous force. A positive Ra_Ω represents the heating case while a negative Ra_Ω is for the case of cooling.

Different scaling quantities in the non-dimensionlization may result in different parameter groups for effects of rotation, curvature and heat/cooling. Here we introduce L_1 and L_2 to represent effects of rotation and heating/cooling, respectively, because they represent ratios of dynamical parameters in the

Coriolis problem and in the mixed-convection problem to the parameter De^2 in the Dean problem. They were found to be two parameters in determining flow patterns in a channel with curvature, rotation and heating/cooling [9], and are introduced in the governing equations (1)–(5) explicitly, since we are mainly concerned with the transition of flow structures in this work. In terms of force ratios, L_1 and L_2 are the ratios of Coriolis force and buoyancy force over centrifugal force, respectively. In particular, L_1 is proportional to $R_c\Omega/W_1$, which may be regarded as a modified rotation number. Note that as they are related to the Dean number, the rotational Reynolds number and the rotational Rayleigh number in a clear way, there should be no difficulty in application of results. In particular, $Ro = 2DkL_1/(3Re)$ and $Ra_\Omega = 16DkL_2$. Here Ro is rotation number defined as $Ro = \Omega a/W_m$.

Boundary conditions may be written, in terms of dimensionless variables, as

$$u = v = w = t = 0 \quad \text{at } r = 0, \quad 1 \quad \text{for} -1 \leqslant z \leqslant 1 \tag{6}$$

$$u = v = w = t = 0 \quad \text{at } z = -1, \quad 1 \quad \text{for } 0 \leqslant r \leqslant 1. \tag{7}$$

After velocity and temperature fields are obtained, computations of local friction factor and Nusselt number are of practical interest. Following the usual definitions, expression for product of friction factor and Reynolds number fRe and Nusselt number Nu can be written, based on local streamwise velocity gradient or temperature gradient at the wall, as

$$fRe = \frac{2}{w_m}\left(\frac{\partial w}{\partial n}\right)_{wall} \tag{8}$$

$$Nu = \frac{1}{t_b}\left(\frac{\partial t}{\partial n}\right)_{wall} \tag{9}$$

in which w_m and t_b are mean streamwise velocity and bulk mean temperature, respectively.

Mean friction factor and Nusselt number can be obtained either by peripherally averaging the local values or by making overall force and energy balance along the axis of channel. The calculated values by these two methods were found to be in good agreement. The result presented in this paper is the average of the values obtained by these two methods.

The governing equations (1)–(5) are solved numerically under the boundary conditions (6) and (7). The numerical scheme is based on the finite volume method which is an adaptation of that in Ref. [10]. Main features of this method include a staggered mesh system, a power-law formulation for the combined effect of convection and diffusion terms, an equation-solving scheme consisting of an alternating direction line-by-line iterative procedure (ADI) with block correction technique, and a well-known SIMPLE scheme for velocity–pressure coupling.

The initial calculation for the Dean problem was performed by setting angular velocity $\Omega = 0$ to verify the code. The results of the present analysis are in excellent agreement with the published theoretical, numerical and experimental results [11]. The computational grid covers the whole cross section of the channel to allow a possible asymmetric solution with respect to the r-axis. Four pairs of grid sizes uniformly distributed in the flow domain were used to check the grid dependence. They are 35×35, 43×43, 51×51 and 59×59. Variations of six representative properties with the grid size are listed in Table 1 for six cases at $L_2 = -18$, -2, -0.71, 0, 2, 10 with $\sigma = 0.02$, $Pr = 0.7$, $Dk = 100$ and $L_1 = 1$. These six cases are chosen because they cover all typical secondary flow patterns obtained in the present work. The general trend of these results as the grid size is decreased tends to indicate that the solution for the case of (51×51) grids are accurate to within 1% tolerance. We also compared the detailed variations of flow and temperature fields for different grid sizes, and found that 51×51 is indeed a reasonably accurate choice for the grid size. The solution was assumed to be convergent in a numerical sense if the maximum relative error in each of the primitive variables (i.e. velocity components, temperature and pressure) over whole grids is less than 10^{-6} between successive iterations.

3. RESULTS AND DISCUSSION

Within the scope of the present study, we focus on the flow transitions due to the buoyancy force whose effect is represented by the parameter L_2. The results shown in this paper are thus confined to a set of fixed values of the other governing parameters. In particular, $\sigma = 0.02$, $Pr = 0.7$, $Dk = 100$ and $L_1 = 1$. For a positive L_1, the rotation is positive with a Coriolis force directed along the positive R-direction on the cross plane.

Instabilities of the physical problem at various orders (secondary and the higher order) would suggest existence of asymmetric solutions with respect to the horizontal centerline in some region of the parameter space, the region with high dynamical parameters in particular. This has been confirmed both numerically and experimentally in the related problems [5, 7, 12–17]. To allow possible asymmetric solutions, we have not imposed a symmetric condition on the horizontal centerline. For the flow region shown in this paper with a low value of dynamic parameters, however, no asymmetric solutions are detected. This allows us to show only the upper half of the cross section. In particular, the left and right frames of each contour figure are the upper half of the inner (convex) and outer (concave) walls, respectively. Also the upper and bottom frames are the upper wall and the horizontal centerline, respectively.

3.1. *Flow transitions and temperature distributions*

3.1.1. *The heating case with* $L_2 \geqslant 0$. The typical secondary flow patterns, streamwise velocity and tem-

Table 1. Variations of six representative properties with grid size at $\sigma=0.02$, $Pr=0.7$, $Dk=100$ and $L_1=1$ [$(fRe)_0=14.23$, $Nu_0=3.608$]

L_2	Grids	De	$\lvert\psi\rvert_{max}$	w_{max}	t_{max}	$fRe/(fRe)_0$	Nu/Nu_0
−18	35×35	46.5	13.595	0.02711	12.024	2.195	2.918
	43×43	46.9	13.622	0.02733	17.230	2.160	2.881
	51×51	47.1	13.600	0.02744	12.343	2.144	2.864
	59×59	47.2	13.608	0.02750	12.351	2.142	2.861
−2	35×35	69.8	7.749	0.04451	30.710	1.458	1.735
	43×43	69.9	7.733	0.04463	30.872	1.449	1.728
	51×51	70.0	7.723	0.04474	30.981	1.444	1.724
	59×59	70.1	7.728	0.04479	31.008	1.441	1.722
−0.71	35×35	96.5	0.9926	0.06912	74.224	1.052	1.048
	43×43	96.5	0.9791	0.06917	74.261	1.049	1.047
	51×51	96.4	0.9662	0.06920	74.284	1.046	1.046
	59×59	96.4	0.9641	0.06921	74.287	1.045	1.046
0	35×35	69.6	6.906	0.04373	31.548	1.456	1.696
	43×43	69.8	6.876	0.04388	31.773	1.447	1.689
	51×51	69.9	6.865	0.04396	31.894	1.441	1.686
	59×59	69.9	6.868	0.04398	31.908	1.438	1.684
2	35×35	57.4	8.335	0.03368	19.827	1.764	2.171
	43×43	57.7	8.322	0.03386	19.984	1.749	2.157
	51×51	57.8	8.293	0.03396	20.114	1.740	2.150
	59×59	57.9	8.288	0.03401	20.125	1.737	2.148
10	35×35	48.0	12.433	0.02708	13.197	2.115	2.735
	43×43	49.8	12.389	0.02731	15.397	2.084	2.707
	51×51	51.9	12.951	0.03101	16.213	1.937	2.491
	59×59	52.0	12.946	0.03109	16.255	1.931	2.488

perature contours are shown in Fig. 2 for several representative values of L_2. In the figure, the stream function, streamwise velocity and temperature are normalized by their corresponding maximum absolute values $|\psi|_{max}$, w_{max} and t_{max}. A star * is drawn to denote the position with these maximum values. A vortex with a positive (negative) value of the stream function indicates a counter-clockwise (clockwise) circulation. Table 2 lists the values of several representative properties, namely, Re, De, $|\psi|_{max}$, w_{max}, t_{max}, mean friction factor ratio, mean Nusselt number ratio and coordinate (x, y) at which $|\psi|$, w and t take their maximum values.

With zero value of L_2, centrifugal-type buoyancy force disappears. Heat transfer is purely forced convection. In the cross plane, both centrifugal (due to curvature) and Coriolis forces (due to the rotation) act along the positive R-direction for the case of positive rotation. Secondary flow consists of one-pair of counter-rotating vortices with a counter-clockwise circulating direction as shown in Fig. 2(a). Fluid in the core region is driven in the positive R-direction by centrifugal and Coriolis forces. The outward flow in the core region forces fluid near the upper and lower walls to flow in the negative R-direction and one pair of counter-rotating vortices is generated. These are so-called Ekman vortices. Strong inward flow near the upper and lower wall is observed and this induces the Ekman layer [Fig. 2(a)] [18].

As L_2 increases from zero, the secondary flow becomes stronger since outward buoyancy force enhances centrifugal and Coriolis forces. However, it consists of the same type of one pair of counter-rotating vortices as shown in Fig. 2(b). There exists a weak secondary flow region in triangular form [Fig. 2(b)] near the central part of outer wall. This foreshadows the onset of an instability to be described later.

Shown in the second row of Fig. 2(a, b) are streamwise velocity isovels corresponding to the secondary flow patterns in the first row. It is observed that the isovels are more sparsely spaced in the region near inner wall than near outer wall. Consequently, pronounced peripheral variations are expected in local friction factors. Densely distributed isovels near the center part of outer wall result in a high pressure region since centrifugal force and Coriolis force are proportional to W^2 and W, respectively. Buoyancy force is also larger in this region because of a larger temperature gradient [the third row of Fig. 2(a, b)]. Flow in the channel core is not geostrophic; it is *ageostrophic*, i.e. pressure gradients are balanced by both body forces and convective inertial force. Two streamwise velocity peaks are observed with one on the upper half of the cross section and the other on the lower half. Regions of maximum velocity are moved toward upper and lower walls while they are shifted toward the outer wall. There is an indication of peak-

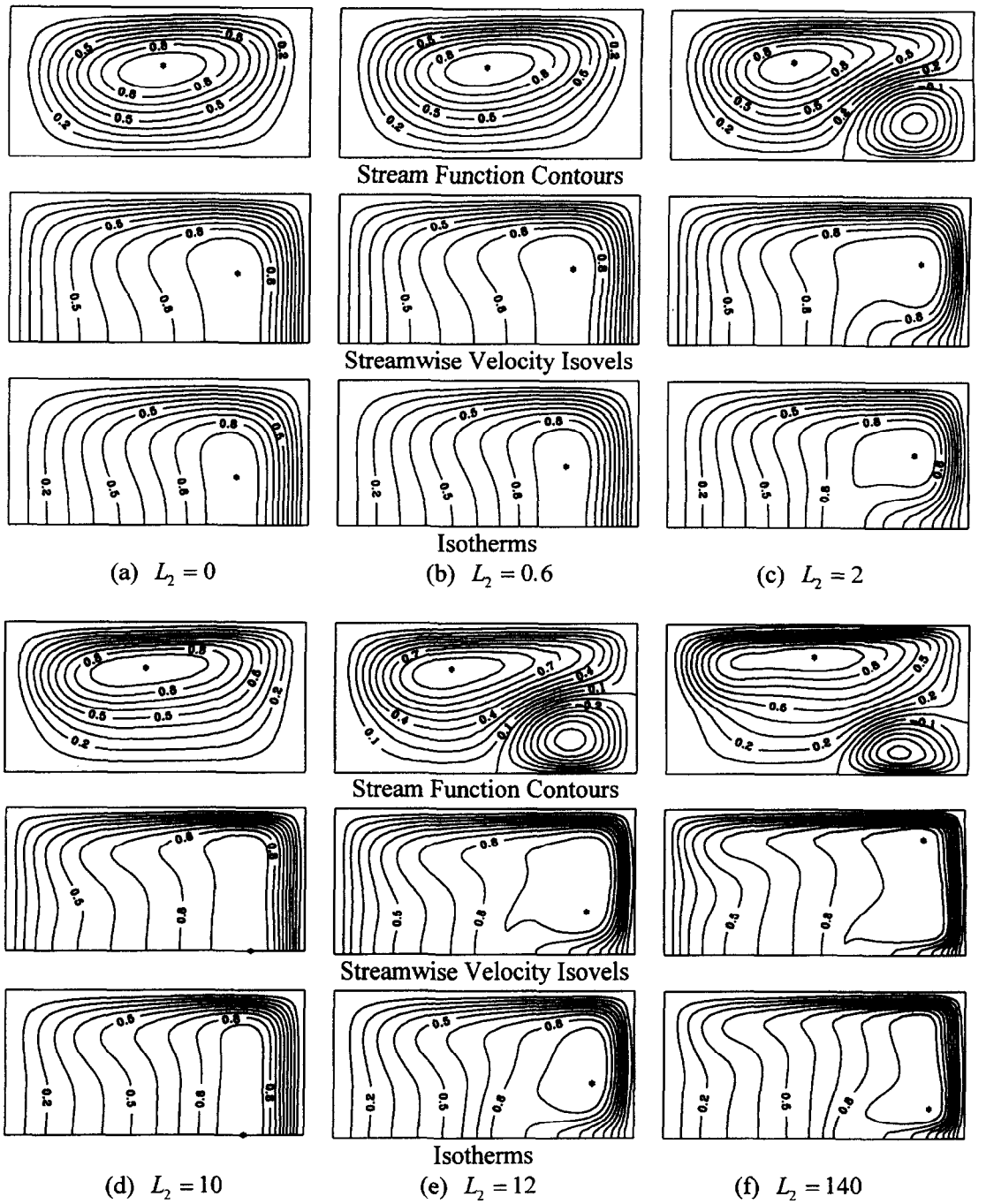

Fig. 2. Buoyancy-force-drive transitions in flow structures and temperature distributions with $L_2 \geqslant 0$ at $\sigma = 0.02$, $Pr = 0.7$, $Dk = 100$ and $L_1 = 1$.

ing of the streamwise velocity near boundary layer regions at the upper and lower walls. The peaking occurs because the boundary layer is being fed by high velocity fluid from the outer wall; the core, however, is being fed by lower velocity fluid from the inner wall. A depression in the streamwise velocity profile near the outer wall foreshadows the onset of an instability to be described later.

Qualitatively similar results are observed for the temperature distribution [the third row of Fig. 2(a, b)]. Pronounced peripheral variations in local Nusselt number result from more sparsely spaced isotherms in the region near the inner wall than near the outer wall. The reason for this is that the larger streamwise velocity gradients exist in the region near the outer wall. Two symmetric (with respect to the horizontal centerline) *high* temperature regions are observed. The physical mechanism can be explained by recalling the secondary flow patterns. A larger inward secondary flow near the upper and lower walls brings relative

Table 2. Variations of several representative properties with L_2 at $\sigma=0.02$, $Pr=0.7$, $Dk=100$ and $L_1=1$ ($(fRe)_0=14.23$, $Nu_0=3.608$)

L_2	Re	De	$\lvert\psi\rvert_{max}$ (x,y)	w_{max} (x,y)	t_{max} (x,y)	$fRe/(fRe)_0$	Nu/Nu_0
−145	256	36.2	21.706 (0.51,0.391)	0.02137 (0.14,0.396)	6.981 (0.14,0.375)	2.789	3.939
−18	333	47.1	13.6000 (0.612,0.348)	0.02744 (0.12,0.313)	12.34 (0.14,0.188)	2.144	2.864
−17	362	51.2	13.772 (0.510,0.348)	0.03189 (0.18,0)	15.33 (0.18,0)	1.971	2.616
−6	389	55.1	9.624 (0.592,0.326)	0.03293 (0.14,0.292)	17.60 (0.16,0.25)	1.834	2.346
−2	495	70.0	7.723 (0.429,0.304)	0.04474 (0.22,0.229)	30.98 (0.22,0.188)	1.444	1.724
−0.71	682	96.4	0.9662 (0.755,0.152)	0.0692 (0.5,0)	74.28 (0.5,0)	1.046	1.046
0	494	69.9	6.865 (0.510,0.304)	0.04396 (0.76,0.229)	31.89 (0.76,0.1667)	1.441	1.686
0.6	466	65.9	7.985 (0.490,0.304)	0.04087 (0.78,0.25)	27.65 (0.76,0.208)	1.526	1.826
2	409	57.8	8.293 (0.408,0.326)	0.03396 (0.84,0.271)	20.11 (0.82,0.25)	1.740	2.150
10	367	51.9	12.95 (0.469,0.348)	0.03101 (0.82,0)	16.21 (0.8,0)	1.937	2.491
12	336	47.6	12.926 (0.388,0.348)	0.02680 (0.84,0.146)	12.88 (0.86,0.188)	2.112	2.765
140	247	35.0	22.198 (0.490,0.391)	0.01930 (0.86,0.396)	6.658 (0.88,0.104)	2.878	3.964

cold (i.e. non-dimensional temperature close to zero) fluid to the inner wall; the colder fluid near the inner wall returns to the core region of the channel, flows outward and isolates the warmer fluid in the upper and lower sides of the channel. Also, fairly uniform outward secondary flow in the core region leads to a flattened isotherm distribution in that region.

Qualitatively similar streamwise velocity and temperature distributions in Figs. 2(a, b) imply that Coriolis terms in the streamwise momentum equation are not strong enough. It is the secondary flow that makes the streamwise velocity and temperature profiles different from the parabolic profile in Poiseuille flow. Effect of the secondary flow enters the governing equation for the main flow through three terms: convection term, and two Coriolis terms due to the curvature and rotation, respectively. Effect of the secondary flow enters the energy equation through one term only, i.e. convection term. When the Coriolis terms in the streamwise momentum equation are too weak to modify main flow effectively, main flow and temperature distributions should be qualitatively similar. However, they might have qualitatively different distributions if the Coriolis force is strong enough.

When buoyancy force becomes stronger, the ageostrophic one-pair vortex breaks down into a configuration of two pairs of counter-rotating vortices that are asymmetric with respect to the vertical centerline of the channel [Fig. 2(c)]. The additional pair of clockwise circulating vortices located in the center of outer wall are called *buoyancy vortices*. They result from a buoyancy force instability and are similar to the *Dean vortices* due to the centrifugal instability. A strong inward secondary flow exists between these two vortices and a strong outward secondary flow appears between the original larger vortices (*Ekman vortices*) and the smaller vortices (*buoyancy vortices*).

Onset of the *buoyancy vortices* is consistent with the instability explanation in Ref. [19] for the Dean problem. In the region near the central outer wall, the pressure gradient across the channel in R-direction is positive, but centrifugal, Coriolis and buoyancy forces decrease from a maximum value to zero at the outer wall. Instability due to an imbalance between pressure gradient inwards and body forces outwards results in an unstable region. If the buoyancy force becomes large enough, viscous effects can no longer hold the one-pair vortex structure in place, thus additional vortices may appear. The resulting secondary flow is similar to those in Ref. [19] for the Dean problem and in Ref. [20] for the Coriolis problem. However, the instability here is caused by all three body forces rather than by centrifugal force (Coriolis force) alone, as in the Dean problem (Coriolis problem). Since no such instability can exist in the absence of the buoyancy force [Fig. 2(a)], we may still call this instability the buoyancy force instability, and the resulting additional pair of vortices the buoyancy vortices.

The second row of Fig. 2(c) demonstrates the way in which buoyancy vortices affect isovels of the streamwise velocity. Significantly distorted isovels are observed in the region with the buoyancy vortices. Corresponding to the strong inward secondary flow, the isovels in that region are moved inwards by the buoyancy vortices. Two symmetric high velocity cores are found with respect to the horizontal centerline.

Position of the maximum streamwise velocity, at which the centrifugal and Coriolis forces are maximum, is located on the boundary line between Ekman and buoyancy vortices. It is clear that the buoyancy force becomes driving force for the secondary flow. Comparing with those in Fig. 2(a, b), the isovels in the region near upper and lower wall are more tightly spaced. Large velocity gradients are also found between each of two high velocity cores and the outer wall. Thus the higher local friction factors are expected there.

The third row of Fig. 2(c) shows that buoyancy vortices significantly affect isotherms. The isotherms are drastically distorted inward near the center of outer wall where the buoyancy vortices occur. Two symmetric high temperature cores (with respect to the horizontal centerline) appear in the cross plane. Isotherms in the regions near upper and lower walls are more tightly spaced than those shown in Fig. 2(a, b). Larger temperature gradients are also found between each of two high temperature cores and the outer wall. Thus a higher heat transfer rate is expected in these regions.

If buoyancy force is now increased to that with $L_2 = 10$, the buoyancy vortex pair presented in Fig. 2(c) disappears and the secondary flow restabilizes to a slightly asymmetric one-pair vortex configuration, as shown in Fig. 2(d). This is similar to that of Coriolis vortices [11], and shows that the primary buoyancy force instability in forms of buoyancy vortices could be cancelled by increasing buoyancy force. The streamwise velocity profile assumes a Taylor–Proudman configuration in the core region with a maximum located on the horizontal centerline [Fig. 2(d)]. Tightly spaced isovels along outer wall, upper and lower walls signal the high local friction factors in these regions. Similarity between streamwise velocity and temperature profiles still holds, although the difference between them becomes larger than the previous cases.

It is worth noting that near uniformity of streamwise velocity in the core region of rotating curved channels is of great importance in aerosol centrifuges. It allows aerosol centrifuges to function as true particle spectrometers [21, 22].

When buoyancy force is increased further, however, buoyancy vortices reappear and remain in a large portion of the parameter space [Fig. 2(e, f)]. This has not been observed for the Coriolis vortices [11]. Here the buoyancy vortices [Fig. 2(e, f)] are smaller than those in Fig. 2(c). It appears that this is the first numerical calculation to illustrate reappearance of buoyancy vortices upon increasing the buoyancy force further. Note that streamwise velocity and temperature distributions become qualitatively similar to those in Fig. 2(c), while a quantitative difference exists between them.

3.1.2. *The cooling case with* $L_2 < 0$. If fluid is cooled, an inward buoyancy force counteracts centrifugal and Coriolis forces in the cross plane. The flow situation is more complicated. Figure 3 shows some typical secondary flow patterns, streamwise velocity isovels, and isotherms with a negative value of L_2.

For a small value of $|L_2|$, effect of the buoyancy force is very weak. Flow structure and temperature distribution remain basically similar to those in Fig. 2(a). If the $|L_2|$ is increased further such that the buoyancy force is of the same order of magnitude as the centrifugal and Coriolis forces, two-pair clockwise circulating vortices occur and grow near the inner and outer walls. Thus the secondary flow appears to be multi-pair vortices with co-existence of counter-clockwise circulating Ekman vortices and clockwise circulating vortices near both inner and outer walls. Formation of these clockwise circulating vortices significantly changes flow structure and temperature distribution, in particular, the Ekman vortices are squeezed to the center part of cross plane with a dramatic change in their size and shape. The strength of secondary flow is significantly reduced (Table 2), and streamwise main flow and temperature profiles are essentially axisymmetric and parabolic with the maximum value occurring along the horizontal centerline at or very close to the center of cross plane [Fig. 3(a)]. In this flow region, secondary flow is too weak to modify main flow and temperature distributions effectively. The inertial force due to the secondary flow is very weak as compared with the viscous force. Driving force for the main flow (i.e. pressure term) is mainly balanced by the viscous force in whole flow domain. Other forces (inertial and combine body force) are very weak. Flow in the channel core is neither ageostrophic nor geostrophic. Viscosity effect is not confined in a thin layer along the walls, but exists in the whole cross section of the channel. Consequently, the integral-type method developed in Refs. [1, 2] is clearly not valid in analyzing this structure. Note that no counter-part exists in the cases with $L_2 \geqslant 0$. However, similar results were also found for the case of circular cross section using a perturbation method [9].

When two or more body forces are directed in opposite direction and almost cancel each other, there are two potentially unstable regions alternating with two stable regions [7]. The secondary flow was experimentally observed as multiple pairs of vortices which are very similar to that in Fig. 3(a) [7].

Upon increasing buoyancy force further, further growth of clockwise circulating vortices finally causes original Ekman vortices to disappear and the secondary flow becomes a one-pair vortex structure with a clockwise direction of the circulation, as shown in Fig. 3(b). This shows that flow reversal can result from an inward buoyancy force, and the reverse direction of secondary flow indicates the domination of the buoyancy force

Figure 4 illustrates this reversal process. Upon increasing buoyancy force, clockwise circulating vortices grow, squeeze Ekman vortices, push Ekman vor-

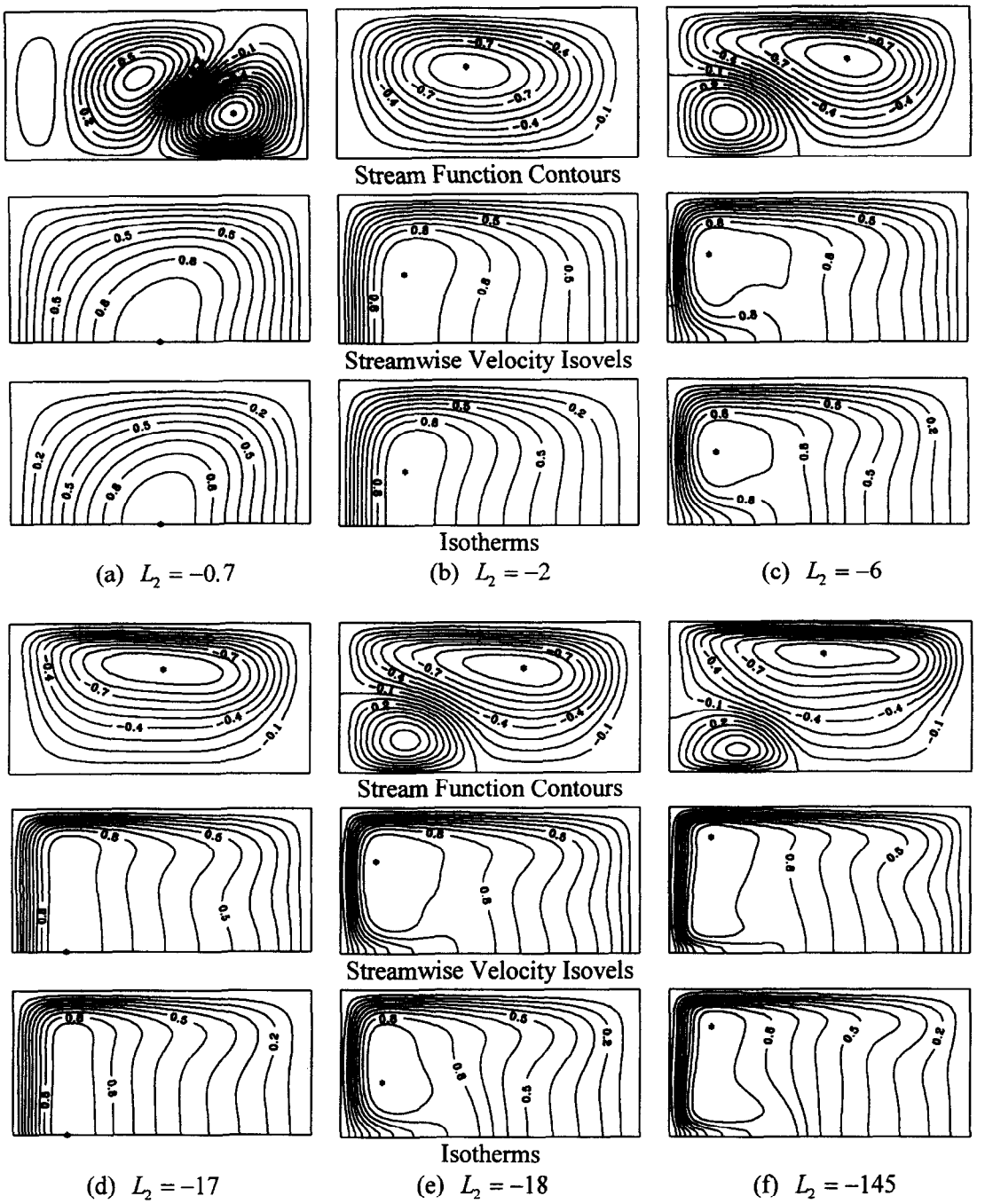

Fig. 3. Buoyancy-force-driven transitions in flow structures and temperature distributions with $L_2 < 0$ at $\sigma = 0.02$, $Pr = 0.7$, $Dk = 100$ and $L_1 = 1$.

tices to the upper and lower walls, and merge together to kill the Ekman vortices and finish the reversal process. Note that the resulting clockwise circulating one-pair vortex flow structure [Fig. 3(b)] is qualitatively similar to that in Fig. 2(a) by interchanging the inner wall and outer wall. This is also true for the temperature distribution. In particular, isovels and isotherms are observed to be more tightly spaced near the inner wall than near the outer wall. This generates a high pressure region near the inner wall. Flow in the channel core appears ageostrophic. Two main velocity peaks and temperature peaks are seen near the inner wall rather than the outer wall with one on the upper half of cross plane and the other on the lower half. The regions with higher velocity and temperature are moved toward the upper and lower walls while they are shifted toward the inner wall by an inward buoyancy force. A depression in the main velocity profile near the inner wall foreshadows onset of an instability.

Upon increasing buoyancy force further, a buoy-

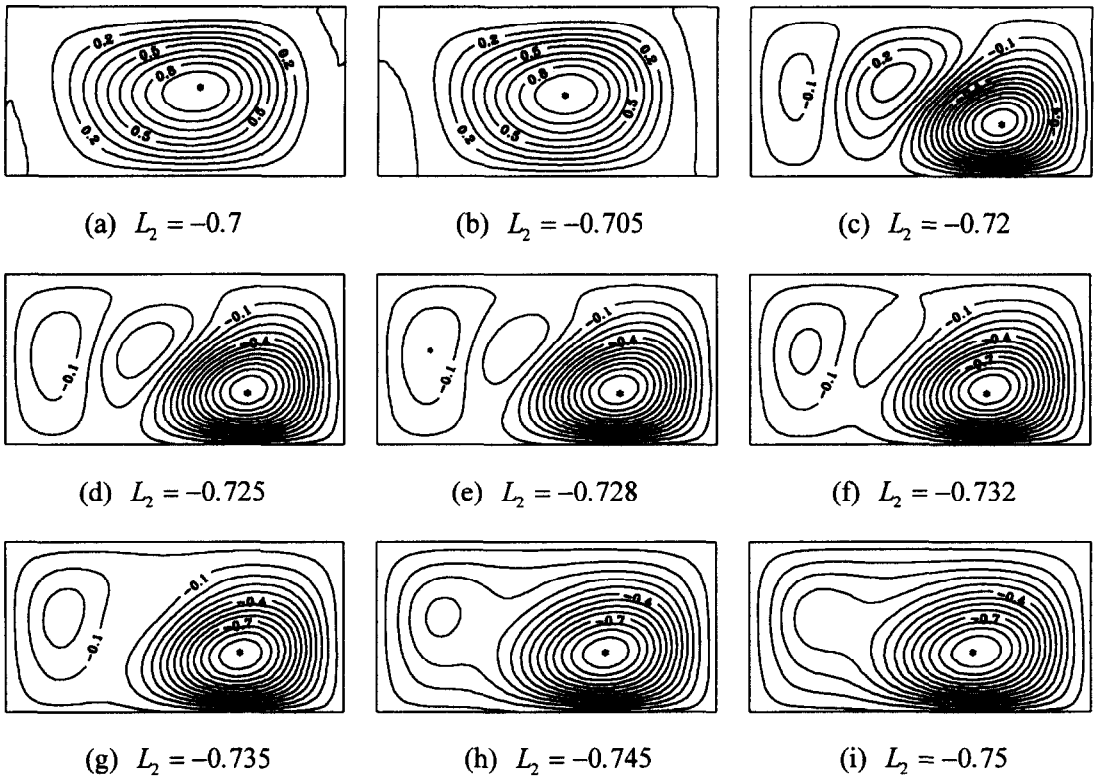

Fig. 4. Secondary flow reversal due to the inward buoyancy force.

ancy force instability sets up in forms of buoyancy vortices on the inner wall [Fig. 3(c)]. Flow structure and temperature distributions become qualitatively similar to those in Fig. 2(c) by interchanging inner wall and outer wall. Upon increasing the value of $|L_2|$ even more, the buoyancy instability in forms of the buoyancy vortices on the inner wall is cancelled completely. Secondary flow restabilizes to a slightly asymmetric one-pair vortex structure [Fig. 3(d)] which is qualitatively similar to that in Fig. 2(d). Streamwise velocity assumes a Taylor–Proudman configuration with a maximum located on the horizontal centerline. A similar profile is also observed for the temperature.

Similar to the heating case, reappearance of the buoyancy force instability is observed upon increasing inward buoyancy force further [Fig. 3(e, f)]. This leads to a flow structure and temperature distribution [Fig. 3(e, f)] qualitatively similar to those in Fig. 2(e, f) through interchanging inner wall and outer wall. It is interesting to note that the buoyancy vortices with a larger value of $|L_2|$ are smaller in size. This can be inferred from the buoyancy vortices shown in Figs. 2 and 3.

3.2. *The distributions of friction factor and Nusselt number*

Distributions of friction factor and Nusselt number along upper half of inner wall, upper wall and upper half of outer wall, are illustrated in Fig. 5(a)–(f). They are shown on the basis of values for a stationary straight channel [$(fRe)_0 = 14.23$ and $Nu_0 = 3.608$] to facilitate the understanding of variations. The distributions are plotted for six values of L_2 ranging from 0 (curve 0) to -18 (curve 5) at $\sigma = 0.02$, $Pr = 0.7$, $Dk = 100$ and $L_1 = 1$. The corresponding flow structures and temperature distributions are illustrated in Figs. 2 and 3. It is noted that a similarity exists between fraction factor and Nusselt number ratios. This results from the similarity between main flow and temperature distributions (Figs. 2 and 3). Also observed is a similarity between Curve 0 and Curve 2 by interchanging inner wall and outer wall. This is in agreement with the similar main flow and temperature distributions for two cases as discussed in the last section.

Curve 1 illustrates friction factor and Nusselt number ratio associated with the multi-pair vortex structure in Fig. 3(a). In general, the ratios are lower than the other structures. This contributes to a weak secondary flow due to the counteraction of buoyancy force on centrifugal and Coriolis forces. Friction factor (Nusselt number), along the inner wall, decreases monotonously from the center to the upper wall [Fig. 5(a, d)]. This contributes to an impinging effect on the inner wall near the center part and a retreating effect near the upper wall by the clockwise circulating vortices. The shift of isovels and isotherms towards the outer wall [Fig. 3(a)] leads the friction factor (Nusselt number) peak (along the upper wall) away from the center to the outer wall [Fig. 5(b, e)]. The impinging

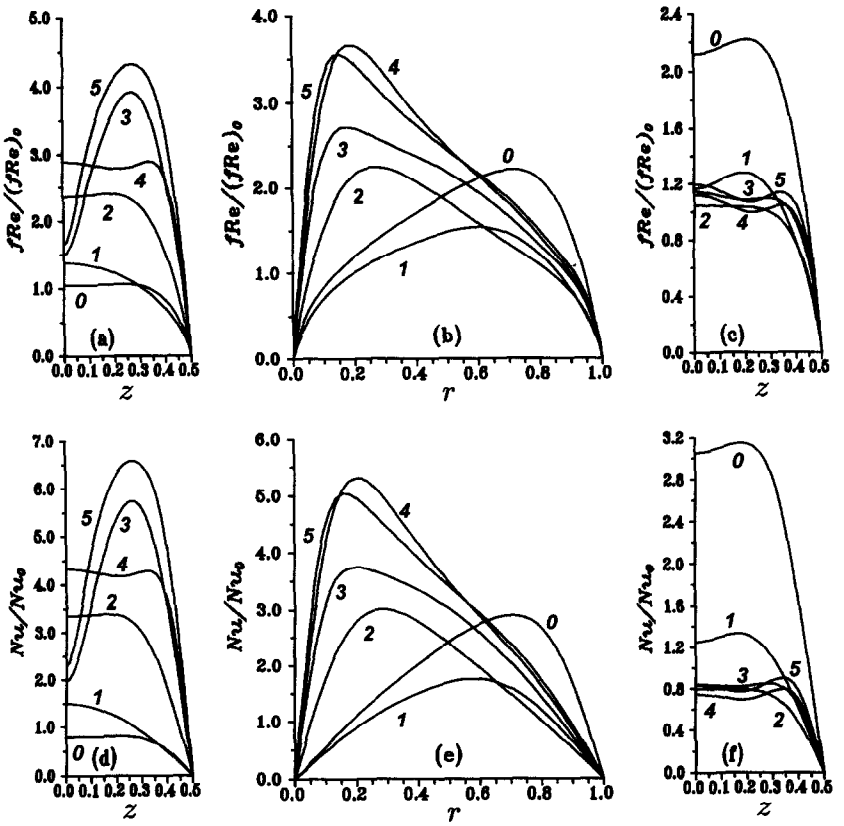

Fig. 5. Effects of flow transitions on local friction factor and Nusselt number at $\sigma = 0.02$, $Pr = 0.7$, $Dk = 100$ and $L_1 = 1$. (a)–(c) Friction factor distributions along the inner, upper and outer walls; (d)–(f) Nusselt number distributions along the inner, upper, and outer walls; curves 0–5 correspond to $L_2 = 0$, -0.71, -2, -6, -17 and -18.

and retreating effects of the clockwise circulating vortices along the outer wall [Fig. 3(a)] generate a local friction factor (Nusselt number) peak along the outer wall [Fig. 5(c, f)].

Curve 2 illustrates friction factor and Nusselt number ratio corresponding to one-pair ageostrophic vortex flow in Fig. 3(b). Densely spaced isovels (isotherms) near the inner wall lead to a higher friction factor (Nusselt number) along the inner wall than those along the outer wall. Relatively uniform distribution of isovels (isotherms) along the center part of inner wall and outer wall generates a region with nearly constant friction factor (Nusselt number) [Fig. 5(a, c, d, f)]. Shift of the regions with maximum streamwise velocity (temperature) towards the inner wall leads to a fiction factor (Nusselt number) distribution, along the upper wall, with a peak near the inner wall [Fig. 5(b, e)].

The buoyancy vortices are of importance in the fundamental research of roll-cell instabilities. They also change flow resistance and heat transfer characteristics significantly. Curve 3 shows friction factor and Nusselt number ratios with the buoyancy vortices in secondary flow [Fig. 3(c)]. The asymmetry of the buoyancy vortices, with respect to the vertical centerline, leads to different distributions of friction factor and Nusselt number at the inner wall from those at the outer wall. A large velocity (temperature) gradient between high velocity (temperature) core and the inner wall [Fig. 3(c)] results in a peak of local friction factor (Nusselt number) in that region along the inner wall. A low friction factor (Nusselt number) region is observed in the center of inner wall. This is induced by the outerwash isovels (isotherms) in that region. Quite uniform streamwise velocity (temperature) along the outer wall leads to a nearly constant local friction factor (Nusselt number) over a wide region of the outer wall. Friction factor (Nusselt number) along the upper wall reaches a peak near the inner wall because a large velocity (temperature) gradient exists between high velocity (temperature) core and the upper wall as shown in Fig. 3(c).

Shown by Curve 4 in Fig. 5(a–f) are friction factor (Nusselt number) distributions from the one-pair geostrophic vortex flow in Fig. 3(d). They are qualitatively similar to those (Curve 2) for the one-pair ageostrophic vortex flow, but with a larger value. The other two differences are: (1) the appearance of a wavy profile along the inner and outer walls; and (2) the extension of region with the nearly constant values of friction factor and Nusselt number [Fig. 5 (a, c, d, f)]. When the flow changes to that in Fig. 3(e) due

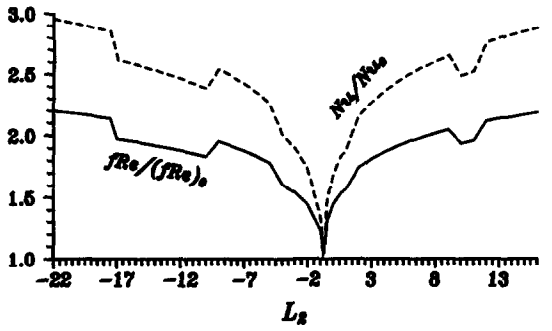

Fig. 6. Variations of mean friction factor and Nusselt number with L_2 at $\sigma = 0.02$, $Pr = 0.7$, $Dk = 100$ and $L_1 = 1$.

to the reappearance of buoyancy vortices, profiles of friction factor and Nusselt number become similar to those denoted by Curve 3, but with a larger value.

Figure 6 shows mean friction factor and Nusselt number represented by solid and dotted lines, respectively. They are plotted in the form of $fRe/(fRe)_0$ and Nu/Nu_0 against L_2 at $\sigma = 0.02$, $Pr = 0.7$, $Dk = 100$ and $L_1 = 1$. It is noted that flow transitions significantly affect the mean friction factor and Nusselt number. Transitions from one-pair vortex structures to two-pair structure due to the appearance and reappearance of buoyancy vortices always substantially increase the friction factor and Nusselt number. A significant decrease is also associated with flow transitions from two-pair vortex structures to one-pair structures due to the disappearance of the buoyancy vortices. This results in uneven variation of friction factor and Nusselt number with the L_2. This effect is also more appreciable for the Nusselt number. When flow is in the region where centrifugal, Coriolis and buoyancy forces just neutralize each other, both friction factor and Nusselt number approach those values for forced convection in a stationary straight channel. This is because the secondary flow becomes weaker due to impaired interaction among the forces. An interesting feature about the mean friction factor and Nusselt number in this flow region is that their ratios, with respect to those for the stationary straight channel, can never be less than 1.

Friction factor ratio and Nusselt number ratio in Fig. 6 can be compared from the point of view of practical engineering. Nusselt number ratio is always higher than that of the friction factor. Also, the variation of Nusselt number with L_2 is more appreciable than that of friction factor.

4. CONCLUDING REMARKS

The rotation and heating/cooling of a channel introduce a buoyancy force in the fluid. Such a body force has significant effects on flow structures and heat transfer through flow reversal, appearance, disappearance and reappearance of the buoyancy vortices. The flow can thus be: (1) one-pair vortex flow with an ageostrophic, virtually inviscid core; (2) one-pair vortex flow with a geostrophic core; (3) two-pair vortex with the buoyancy vortices; or (4) multi-pair vortex flow with a very weak strength of the secondary flow. The circulating direction of the one-pair counter-rotation vortices can be either clockwise or counter-clockwise depending on the value of L_2. Also the buoyancy vortices can appear either near the outer concave wall or the inner convex wall depending on heating or cooling.

Buoyancy force instability in the form of buoyancy vortices can be completely cancelled, and reappear upon increasing the buoyancy force in both inward and outward directions. When the fluid is cooled, inward buoyancy forces cause the direction of the secondary flow to reverse by overcoming the centrifugal and Coriolis forces in the cross plane. The flow reversal occurs by passing through a multi-pair vortex flow region where overall the effect of buoyancy force just neutralizes those of centrifugal and Coriolis forces. Also, a higher inward buoyancy force could lead the buoyancy vortices to appear on the inner convex channel wall.

Friction factor and Nusselt number are significantly affected by flow transitions. In particular, the buoyancy vortices substantially change distributions of local friction factor and Nusselt number with a remarkable increase in their mean values. A very weak secondary flow in forms of multi-pair vortices leads both friction factor and Nusselt number to approach those values for forced convection in a stationary straight channel.

Acknowledgement—This work was supported in part by the Natural Sciences and Technology Board of Singapore.

REFERENCES

1. H. Ludwieg, Die ausgebildete kanalströmung in einem rotierenden system, *Ing.-Arch.* **19,** 296 308 (1951).
2. L. M. Hocking, Boundary and shear layers in a curved rotating pipe, *J. Math. Phys. Sci.* **1,** 123–136 (1967).
3. H. Miyazaki, Combined free and forced convective heat transfer and fluid flow in a rotating curved circular tube, *Int. J. Heat Mass Transfer* **14,** 1295–1309 (1971).
4. H. Miyazaki, Combined free and forced convective heat transfer and fluid flow in a rotating curved rectangular tube, *J. Heat Transfer* **95,** 64–71 (1973).
5. M. Selmi, K. Nandakumar and W. H. Finlay, A bifurcation study of viscous flow through a rotating curved duct, *J. Fluid Mech.* **262,** 353–375 (1994).
6. O. J. E. Matsson and P. H. Alfredsson, The effect of spanwise system rotation on Dean vortices, *J. Fluid Mech.* **274,** 243–265 (1994).
7. L. Wang and K. C. Cheng, Flow in curved channels with a low negative rotation speed, *Phys. Rev. E* **51,** 1155–1161 (1995).
8. W. D. Morris, *Heat Transfer and Fluid Flow in Rotating Coolant Channels* (1st Edn), pp. 27–31. Research Studies Press, Wiley, Chichester (1981).
9. L. Wang and K. C. Cheng, Flow transitions and combined free and forced convective heat transfer in a rotating curved circular tube, *Int. J. Heat Mass Transfer* **39,** 3381–3400 (1996).
10. S. V. Patankar, *Numerical Heat Transfer and Fluid Flow* (1st Edn). Hemisphere, New York (1980).

11. L. Wang and K. C. Cheng, Flow transitions and combined free and forced convective heat transfer in rotating curved channels: the case of positive rotation, *Phys. Fluids* **8,** 1553–1573 (1996).
12. S. R. Sankar, K. Nandakumar and J. H. Masliyah, Oscillatory flows in coiled square ducts, *Phys. Fluids* **31,** 1348–1358 (1988).
13. K. Nandakumar, H. Raszillier and F. Durst, Flow through rotating rectangular ducts, *Phys. Fluids A* **3,** 770–781 (1991).
14. K. Nandakumar and H. J. Weinitschke, A bifurcation study of mixed-convection heat transfer in horizontal ducts, *J. Fluid Mech.* **231,** 157–187 (1991).
15. Y. Guo and W. H. Finlay, Splitting, merging and wavelength selection of vortices in curved and/or rotating channel flow due to Eckhaus instability, *J. Fluid Mech.* **228,** 661–691 (1991).
16. K. C. Cheng and L. Wang, Secondary flow phenomena in rotating radial straight pipes, *Int. J. Rotating Mach.* **2,** 103–111 (1995).
17. L. Wang and K. C. Cheng, Visualization of flows in curved channels with a moderate or high rotation speed, *Int. J. Rotating Mach.* (in press).
18. E. M. Smirnov, Asymptotic drag formulas for the rapidly rotating radial channels of rectangular cross section, *Izv. Akad. Nauk. SSSR. Mekh. Zhidk. Gaza*, 42–49 (1978).
19. K. C. Cheng, R. C. Lin and J. W. Ou, Fully developed laminar flow in curved rectangular channels, *J. Fluids Engng* **98,** 41–48 (1976).
20. C. G. Speziale, Numerical study of viscous flow in rotating rectangular ducts, *J. Fluid Mech.* **122,** 251–271 (1982).
21. M. D. Hoover and W. Stöber, Model of particle deposition in spinning duct aerosol centrifuges, *J. Aerosol Sci.* **12,** 223–232 (1981).
22. M. D. Hoover, W. Stöber and G. Morawietz, Experiment on laminar flow in a rotating, curved duct of rectangular cross section, *J. Fluids Engng* **106,** 38–44 (1984).